mater.scichina.com link.springer.com Published online 28 February 2022 | https://doi.org/10.1007/s40843-021-1934-x

Nano-amorphous–crystalline dual-phase design of $Al_{80}Li_5Mg_5Zn_5Cu_5$ multicomponent alloy

Hongzhen Li[1], Chao Yang[2], Jianan Fu[1], Weisi Cai[2], Yuqiang Yan[3] and Jiang Ma[1*]

ABSTRACT **The design of metallic materials with high strength, high ductility, and high thermal stability has always been a long-sought goal for the materials science community. However, the trade-off between strength and ductility remains a challenge. Here, we proposed a new strategy to design and fabricate bulk amorphous–crystalline dual-phase superior alloys out of the $Al_{80}Li_5Mg_5Zn_5Cu_5$ multicomponent alloy. The nano-amorphous phase revealed unexpected thermal stability during fabrication and mechanical testing above the crystallization temperature. The true fracture strength of the $Al_{80}Li_5Mg_5Zn_5Cu_5$ nano-amorphous-crystal dual-phase multicomponent alloy was increased from 528 to 657 MPa, and the true strain was increased from 18% to 48%. In addition, the alloy yielded a strength 1.5 times higher than that of the commonly used high-strength aluminum alloys at 250°C. This strategy provided a new approach and concept for the design of high-performance alloys to ensure strength–plasticity balance.**

Keywords: amorphous alloys, nanocrystalline alloys, multicomponent alloy, high-performance alloys

INTRODUCTION

Materials with high strength, great ductility, and high-temperature resistance are ideal for reliability engineering, extreme environmental applications, and energy efficiency [1,2]. However, most metallurgical methods that are used to increase strength often lead to a decrease in ductility because of a trade-off effect between strength and ductility [3–5]. The introduction of second-phase intermetallic compounds (IMCs) is an effective method to improve the strength and high-temperature resistance of alloys [6–8]. However, most IMCs with crystalline structures are inherently brittle, and the inhomogeneity of the microstructure of IMCs under stress loading can easily cause local stress–strain concentration, resulting in microcracks and catastrophic fracture [9]. The refinement of grains to nano/ultrafine grain systems can result in materials with high strength and ductility at ambient temperatures [10–12], but high-temperature properties caused by the introduction of a large number of nonequilibrium defects, such as grain boundaries, often make the material unstable. This trade-off is symbolic in nanocrystalline and amorphous alloys [13–15]. By contrast, the introduction of a nano-amorphous phase has high strength and ductility because of the high compressive strength exhibited by the amorphous size of less than 100 nm [11,12,16,17], and the shear banding phenomenon can be completely suppressed, thereby exhibiting flow behavior in deformation and thermal stability [18,19]. The currently reported nano-amorphous–crystalline dual-phase design has achieved strength–plasticity balance through partial crystallization by annealing amorphous elements [17], prenucleation by adding high-melting-point elements (e.g., tantalum or niobium) followed by rapid quenching [12,20], and embedding of nanocrystals into amorphous aggregates by magnetron sputtering [16]. However, the methods currently used often are limited to the traditional classical composition systems with high glass-forming capacity.

In this work, we report a new strategy for the nano-amorphous–crystalline dual-phase design in the multicomponent alloy (NDMA). Based on the time–temperature–transformation (TTT) curves of classical solidification [21–23], nano-amorphous–crystalline dual-phase $Al_{80}Li_5Mg_5Zn_5Cu_5$ multicomponent alloy with improved strength–plasticity and unrestricted dimensions can be obtained in the non-classical amorphous composition system. In addition, based on the excellent thermal stability of the amorphous phase, the $Al_{80}Li_5Mg_5Zn_5Cu_5$ NDMA exhibits a yield strength of 430 ± 15 MPa, which is 1.5 times higher than that of commonly used high-strength aluminum alloys at 250°C. Our design strategy provides a basis for the wide application of multicomponent alloys and new ideas for the design of new amorphous composites.

EXPERIMENTAL SECTION

Preparation of ND ribbons

The $Al_{80}Li_5Mg_5Zn_5Cu_5$ (atomic percent, at%) multicomponent alloy was produced from elements with a purity of 99.99% in weight percent by vacuum-induction melting. Using $Al_{80}Li_5Mg_5Zn_5Cu_5$ as a prealloyed material in an argon atmosphere and common induction melting and single-roll melt-spinning technology (v = 60 m s^{-1}), the width is approximately 2–4 mm, and the thickness is approximately 20–40 μm.

Powder metallurgy molding NDMA

$Al_{80}Li_5Mg_5Zn_5Cu_5$ NDMA was produced by hot pressing at 400 MPa and 370°C. The powder used was obtained from

[1] Shenzhen Key Laboratory of High Performance Nontraditional Manufacturing, College of Mechatronics and Control Engineering, Shenzhen University, Shenzhen 518060, China
[2] National Engineering Research Center of Near-net-shape Forming for Metallic Materials, South China University of Technology, Guangzhou 510640, China
[3] Songshan Lake Materials Laboratory, Dongguan 523808, China
* Corresponding author (email: majiang@szu.edu.cn)

quenched ribbons after 50 h of ball milling. The powders were first placed in the mold and prepressurized with 1 kN. When the mold temperature reached 100°C, the pressure was increased to 25 kN, and this pressure value continued until the end of hot pressing. When the temperature in the mold cavity reached 370°C, hot pressing was performed in isothermal mode with a dwell time of 3 min. At the end of hot pressing, the sample was purged with argon gas and removed from the cavity. The laboratory was evacuated to approximately 1×10^{-4} Pa prior to hot pressing to minimize the risk of oxygen contamination during hot pressing.

Compression test

Compression tests were performed on a mechanical testing machine (Zwick-Roell z050tew). $Al_{80}Li_5Mg_5Zn_5Cu_5$ NDMA and the as-received samples were 6 mm high and 3 mm in diameter. The specimens were processed using a slow-walker cut, and then the upper and lower surfaces were polished with 1000-grit sandpaper. The strain rate for the compression work was 10^{-3} s^{-1}. During compression, the strain was recorded by a video extensometer. High-temperature compression was performed in a blast chamber, and the temperature of the chamber was measured using a K-type thermocouple. Before the test, the environmental chamber was preheated. When it reached the specified temperature, the compressed sample was placed in the chamber for 5 min. The strength and ductility reported in this paper were the average results of four compression tests.

Transmission electron microscopy

Microstructural and phase analyses were performed using a transmission electron microscope (TEM, FEI Titan Themis) equipped with an energy-dispersive spectroscope (EDS). The entropic alloy samples for TEM observation were prepared on a Dual Beam System (FEI Scios). Specimens for TEM observation were prepared on a double-beam system (FEI Scios), which were all obtained from randomly selected areas. TEM *in situ* heating experiments were performed on a two-sphere differential Cs-corrected TEM (JEM-ARM300F). The *in situ* heating rate was 50°C min^{-1}, and heating was temporarily stopped after each 50°C increase to allow shooting, and shooting was continued until the temperature reached 450°C.

Electron backscatter diffraction (EBSD)

The microstructural evolution in the deformation area of the samples was characterized by EBSD, using the TESCAN MAIA3 scanning electron microscope, equipped with an HKL-EBSD system. The samples were prepared by ion-beam polishing for 1 h at 6.5 kV. The EBSD characterizations were operated with a step size of 0.5–2 μm at 20 kV.

X-ray diffraction (XRD)

Phase identification was determined by XRD using the Rigaku miniflex 600 XRD instrument and Cu Kα radiation with a wavelength of 0.154 nm. The XRD pattern was acquired in a 2θ range of 20°–90° at a scan rate of 4° per minute and a scanning interval of 0.02°.

Density measurement

The weight of the specimen was measured in the air using an electronic balance (Sartorius Quintix35-1CN, measurement accuracy 0.01 mg) and was marked as $W1$. Afterward, the weight of the sample in analytically pure alcohol was measured and marked as $W2$. The density (ρ) of the specimen could be calculated using the formula $\rho = W1 \times \rho 1/(W1-W2)$, where the density of the analytically pure alcohol is 0.790 g mL^{-1}. The density of the as-received is 2.87 g cm^{-3}, and $Al_{80}Li_5Mg_5Zn_5Cu_5$ NDMA is 2.89 g cm^{-3}. Density measurements were repeated five times for each specimen to obtain reliable results.

RESULTS AND DISCUSSION

Design concept

The strategic approach is based on the confusion principle of amorphous alloy formation [24], the multicomponent effect of multicomponent alloys [25,26], and the TTT curve of the classical solidification theory (Supplementary information and Fig. S1) [21,22]. In a single-roller melt-spinning process with a spinning speed (v) of 60–65 m s^{-1} (speeds greater than 65 m s^{-1} have not been attempted because of experimental conditions), the $Al_{80}Li_5Mg_5Zn_5Cu_5$ multicomponent alloy can obtain a nano dual-phase structure. Fig. S2 illustrates the distribution of the nano dual phase. Subsequently, the quenched ribbons were ball-milled into powders, and then the powder was metallurgically molded to obtain large $Al_{80}Li_5Mg_5Zn_5Cu_5$ NDMA using the design route shown in Fig. 1a. Fig. 1b shows the changes of $Al_{80}Li_5Mg_5Zn_5Cu_5$ grain in the design route: pristine grains, grain refinement, and recrystallization, and the element distribution of $Al_{80}Li_5Mg_5Zn_5Cu_5$ NDMA is shown in Fig. S3. Notably, the NDMA is dominated by the dislocation slip generated by the nano dual-phase of the Al-rich (NDA) region during deformation (Fig. S4). Therefore, we primarily focus on the deformation mechanism of the NDA structure. In addition, the Al-poor phase regions are labeled as IMCs.

The result of EBSD further demonstrates grain refinement (Fig. 1c). In addition, the analysis of four samples produced by the process route in Fig. 1a using XRD (Fig. 1d) indicates the absence of phase transformation during fabrication. Moreover, Fig. 1e shows high-resolution TEM (HRTEM) images of the as-received and NDMA samples in the Al-enriched region, indicating their (left) transformation to NDA (right) after the process route of Fig. 1a. Powder metallurgy was used to obtain large sizes; thus, $Al_{80}Li_5Mg_5Zn_5Cu_5$ NDMA can reach the size limitation and achieve large blocks. As shown in Fig. 1f, using the quenched ribbons and powder metallurgy method, a large bulk of $Al_{80}Li_5Mg_5Zn_5Cu_5$ NDMA was formed.

Stability of nano-amorphous–crystalline dual-phase

TEM *in situ* heating experiments provide direct evidence that the NDA in $Al_{80}Li_5Mg_5Zn_5Cu_5$ is stable at high temperatures. The results are presented in Fig. 2a and Fig. S5. For easier observation, light green is used to cover the crystal phase. The disordered structure in NDA remains stable from 25°C to even 400°C, which is higher than the powder metallurgy temperature of 370°C in our design route. That is, the $Al_{80}Li_5Mg_5Zn_5Cu_5$ NDMA maintains the NDA structure even after powder metallurgy. Notably, the amorphous region was based on the Al content, the crystallization temperature of which should be less than 400°C. However, we did not find the crystallization phenomena in the *in situ* TEM observation, indicating the good stability of the amorphous phase. However, when the temperature increases to above 450°C, crystallization occurs in the amorphous region, and fast Fourier transform (FFT) on the

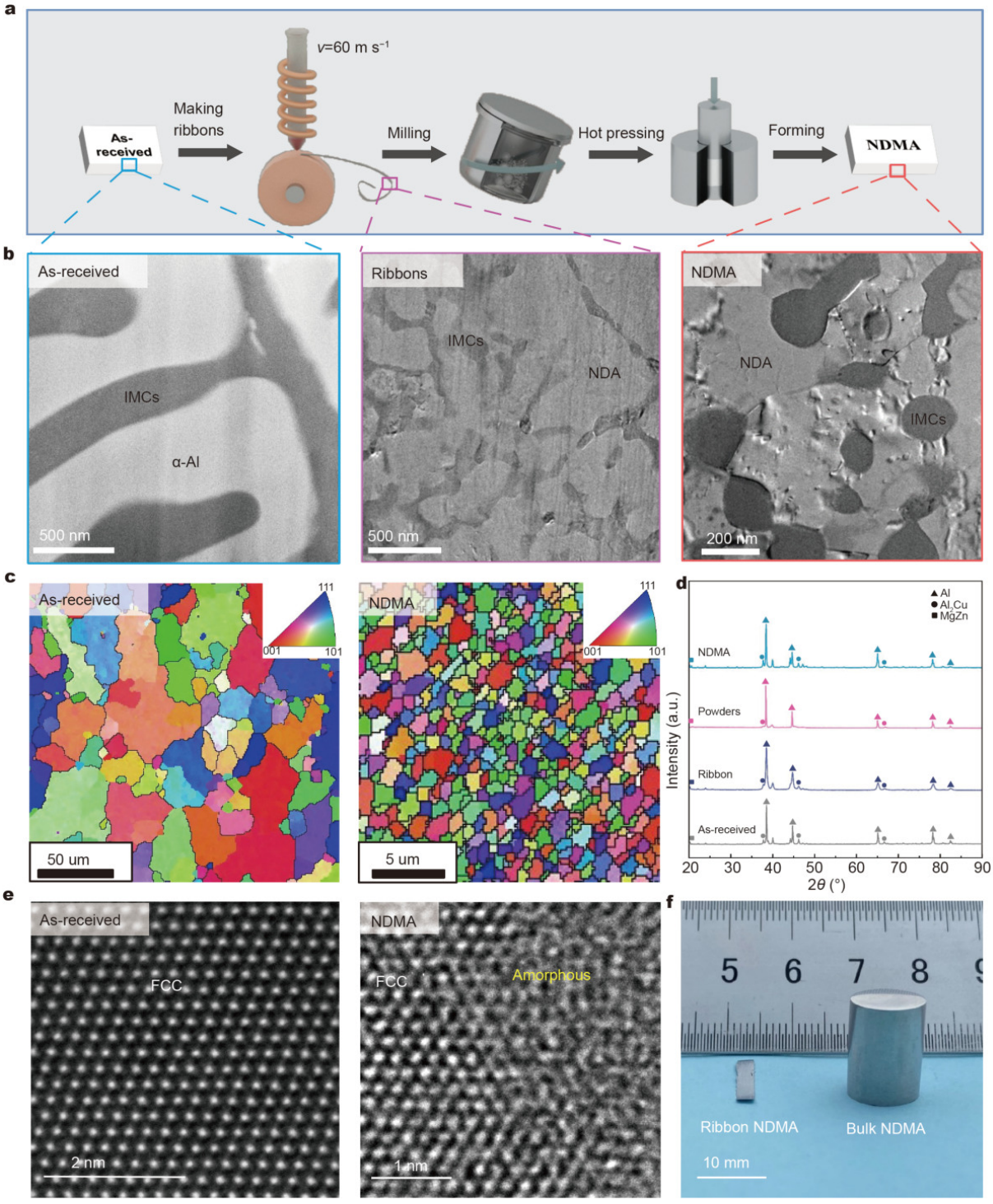

Figure 1 NDMA alloy design strategy route and characterization. (a) NDMA manufacturing diagram; (b) from left to right, the TEM images of the as-received, quenched ribbons, and NDMA; (c) EBSD plot showing the grain structure of the as-received (left) and NDMA (right); (d) XRD images of the as-received, ribbons, powders, and NDMA from manufacturing in (a); (e) HRTEM images of the fcc structure within the α-Al phase of the as-received (left) and NDA of NDMA (right); (f) quenched ribbons (left) and a large bulk of $Al_{80}Li_5Mg_5Zn_5Cu_5$ NDMA (right) from the manufacturing in (a).

right side no longer shows amorphous diffraction rings. The original fcc phase of $Al_{80}Li_5Mg_5Zn_5Cu_5$ has 94.1% Al element and only 1.4% Cu [27,28]. In addition, the Al content is significantly reduced in some regions in the nano dual-phase of the NDA region of $Al_{80}Li_5Mg_5Zn_5Cu_5$ (Fig. 2b). On the contrary, the Cu content is about 7.1%, and it increases significantly in some regions (Fig. 2b, element diagram black shear head), reaching about 22%. Locating the region using HRTEM (Fig. 2b), the Cu content increases to the amorphous phase region, which is more than ten times the 1.4% Cu content of the fcc phase of the as-received sample. This result indicates the presence of Cu with a high melting point, resulting in the amorphous phase and

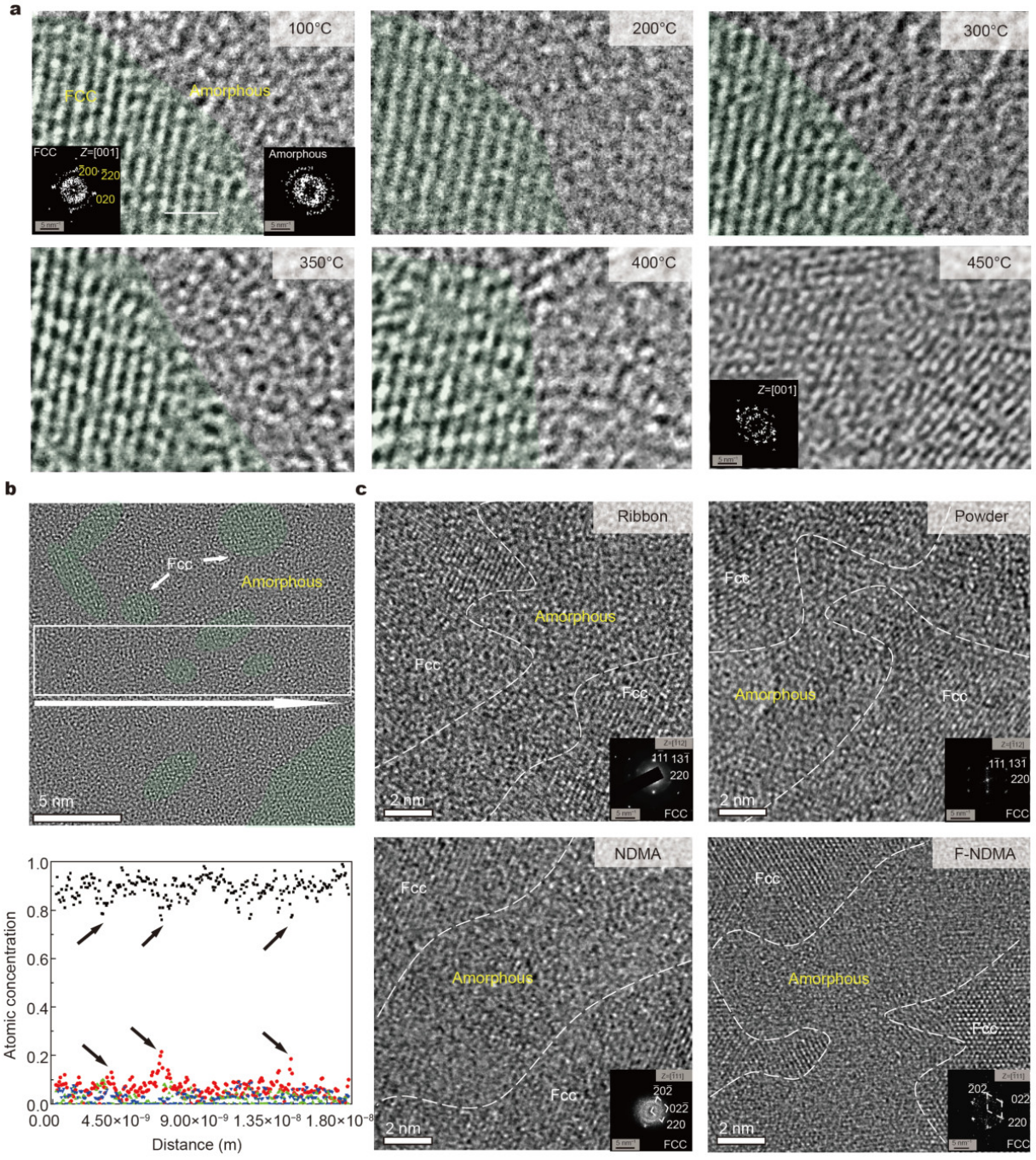

Figure 2 NDA microstructure and thermal stability. (a) *In situ* TEM heating experiments. NDA structures of $Al_{80}Li_5Mg_5Zn_5Cu_5$ NDMA collected during individual heating at 100, 200, 300, 350, 400, and 450°C were imaged under TEM at high resolution. The insets for 100 and 450°C show the FFT results for the corresponding regions, where the left FFT shown at 100°C corresponds to the left fcc, and the right FFT corresponds to the right amorphous. The scale bar is 0.5 nm (see Fig. S5 for the specific location of this region). (b) The HRTEM image of the NDA structure (top): the green coverage area is fcc nanocrystals, and the EDS results of the area surrounded by white wireframe are shown below. (c) The NDA structure is shown for the quenched strips, powder and powder metallurgically formed bulk in the strategic route (Fig. 1a), and NDMA after compression fracture. The FFT in the lower right corner corresponds to the fcc phase structure in the corresponding region.

obtaining high thermal stability. Moreover, the thermal stability of the NDA was further ascertained by the TEM observation of samples at different stages in the strategic route of Fig. 1a. The results are presented in Fig. 2c. The ribbons, powders, bulk sample formed by powder metallurgy, and the fractured specimen after compression kept similar NAD structures, which were generated by single-roll melt spinning.

Mechanical properties

The presence of the nano dual-phase achieves a significant strength–ductility combination and maintains high yield strength at high temperatures. The true stress–strain curve under compression (Fig. 3a) shows that $Al_{80}Li_5Mg_5Zn_5Cu_5$ NDMA has a fracture strength of 657 ± 12 MPa (engineering stress and strain are shown in Fig. S6). However, this trend is not

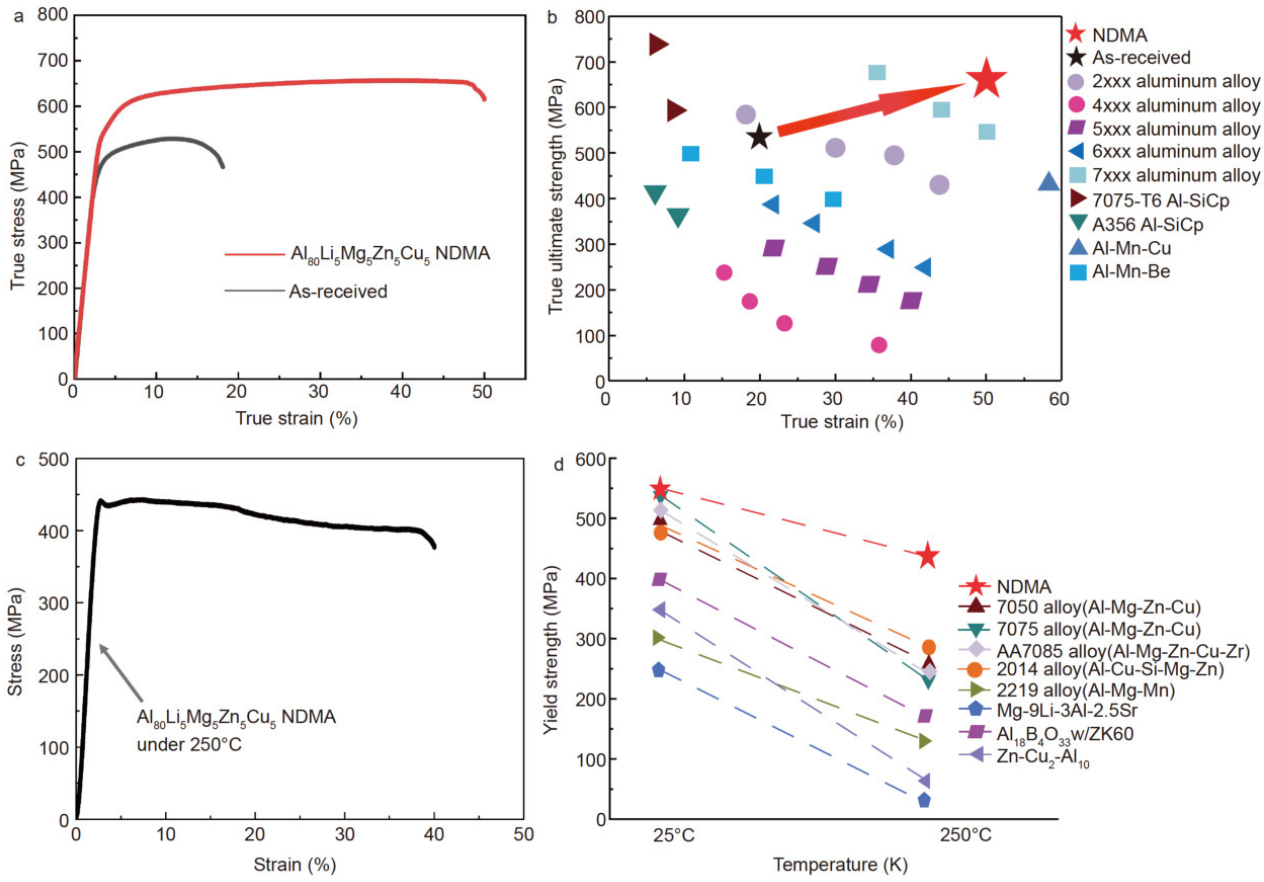

Figure 3 Mechanical properties of $Al_{80}Li_5Mg_5Zn_5Cu_5$ NDMA compared with other alloys. (a) Compression of true stress–strain curves for $Al_{80}Li_5Mg_5Zn_5Cu_5$ NDMA (red) and as-received samples (gray), each with a diameter of 3 mm and a height of 6 mm; (b) comparison of true ultimate strength strain of $Al_{80}Li_5Mg_5Zn_5Cu_5$ NDMA using the compression test results of the as-received, and common aluminum alloys. (c) Engineering stress–strain curve of $Al_{80}Li_5Mg_5Zn_5Cu_5$ NDMA at 250°C, with sample diameter of 3 mm and height of 6 mm. (d) Comparison between yield strength and temperature for $Al_{80}Li_5Mg_5Zn_5Cu_5$ NDMA and other industrial high-strength aluminum alloys.

due to the plastic-forming ability. On the contrary, the true plastic strain of $Al_{80}Li_5Mg_5Zn_5Cu_5$ NDMA increases from 18.34% ± 1.80% in the as-received state to 48.26% ± 2.10% in the $Al_{80}Li_5Mg_5Zn_5Cu_5$ NDMA, with a 2.5-fold increase in plasticity. The increase in strong plasticity at room temperature results from the unique hybrid enhancement mechanism. $Al_{80}Li_5Mg_5Zn_5Cu_5$ NDMA has a significant advantage over other Al alloys in the normal trade-off between true ultimate strength strain (Fig. 3b) [29–33]. However, the excellent thermal stability of NDA allows NDMA to retain its high strength at high temperatures. Fig. 3c shows the compression engineering stress–strain curve for NDMA at 250°C. The yield strength is 430 ± 15 MPa, which is 1.5 times higher than that of industrial high-strength aluminum alloys (Fig. 3d) [34–39]. This result is consistent with the previously described results of thermal stabilization of NDA structures.

The strength–plasticity enhancement obtained by $Al_{80}Li_5Mg_5Zn_5Cu_5$ NDMA is derived from the NDA structure and mixed hard–soft phase strengthening. First, the increase in yield strength (Fig. 3a) is due to grain refinement (Fig. 1c). In general, deformation starts from dislocation sources in adjacent grains [40], and grain refinement leads to an increase in the total area of grain boundaries, resulting in an increase in deformation resistance, which is consistent with the Hall–Petch relationship [41,42]. Based on the "soft–hard model" mechanism [20,43–45], IMCs with $MgZn_2$ as the main component have higher strength than the fcc in the NDA structure.

With the increase of stress applied, dislocation slip is activated from the NDA (soft phase). TEM observation of the $Al_{80}Li_5Mg_5Zn_5Cu_5$ NDMA sample after compression deformation and fracture is shown in Fig. 4a. HRTEM image and Fig. S7 show the region from the upper left inset surrounded by the white dashed line. The fcc grains undergo dislocation deformation at the amorphous–crystalline junction (Fig. 4b, c). The upper and lower insets on the right side of Fig. 4a respectively show the FFT patterns of the #1 and #2 regions (surrounded by the white dashed square in Fig. 4a) in the two nanograins. The one-dimensional (1D) inverse FFT images in Fig. 4b, c reveal the planes of the #1 and #2 regions in Fig. 4a, respectively. Several dislocations found near the boundary between nanocrystals and non-crystals are shown, which are marked with ⊥. In addition, nanocrystals with rotation-dominated deformation are found [47,48]. As shown in Fig. 4d, the nanocrystal undergoes dislocation (red line) with rotational deformation (yellow dashed line) [47,48].

When the size of the amorphous alloys is less than 100 nm, the deformation mode changes from shear band propagation to uniform flow [18,19]. In addition, as the diameter decreases, the

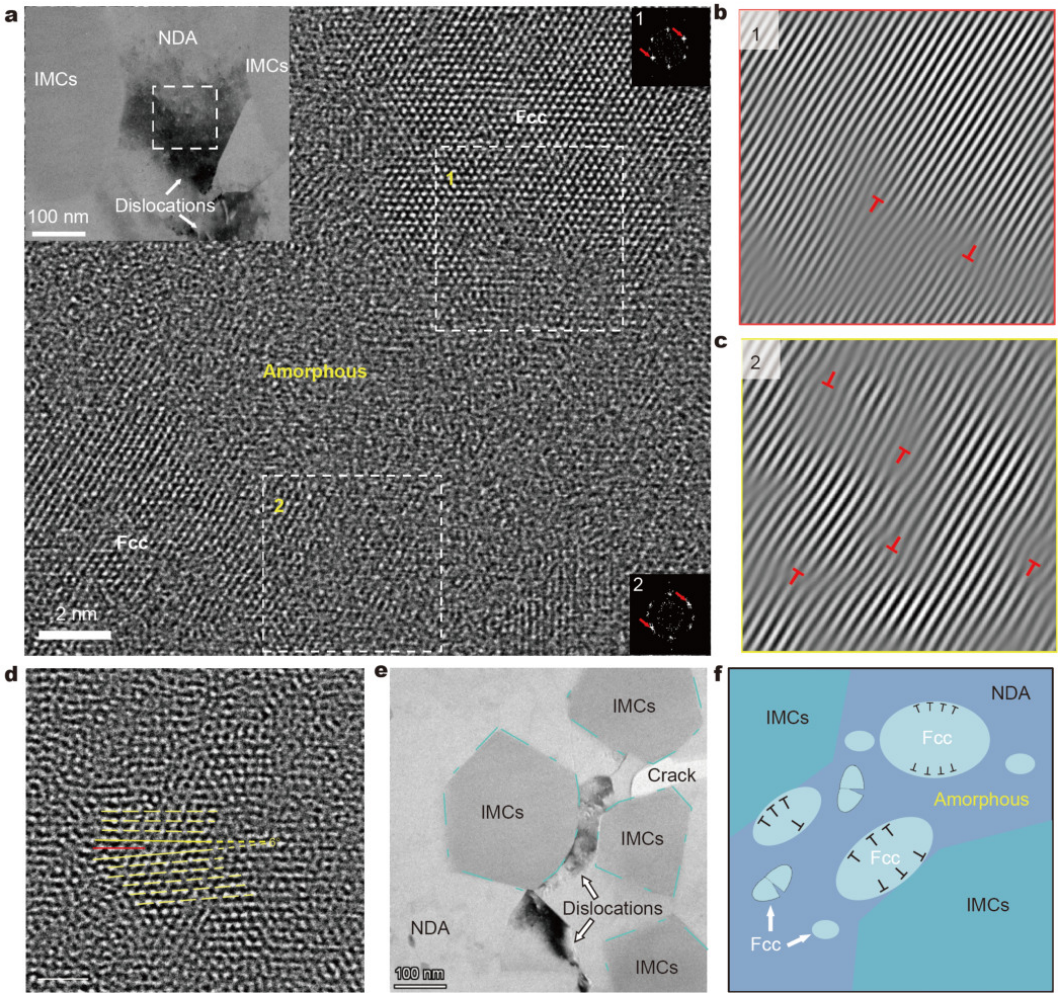

Figure 4 Plastic deformation mechanism of the $Al_{80}Li_5Mg_5Zn_5Cu_5$ NDMA. (a) HRTEM image of the deformed NAD after compression break, with the upper and lower insets on the right corresponding to the FFT patterns in the upper and lower white boxed square regions, respectively. (b and c) 1D Fourier filtered images of the upper and lower Fourier transformed two points (marked by red arrows) in the [46,47] plane (a). Dislocation is marked with ⊥. (d) HRTEM image of the area located in the white square dashed box in the left inset of (a), showing the nanocrystals (grain size of approximately 7 nm) undergoing rotational deformation. The scale bar is 1 nm. (e) TEM image of dislocations in the NDA obstructed by IMCs. (f) Plastic deformation mechanism of $Al_{80}Li_5Mg_5Zn_5Cu_5$ NDMA.

initial stress of the elastoplastic transition is smaller [49]. Therefore, as the load increases, plastic flow increases and begins to occur in the amorphous phase [49]. Moreover, the accumulation of dislocations within NDA is followed by propagation, which is blocked by the hard IMC region [20,43,44]. As shown in Fig. 4e, the dislocations in the NDA (dark region within NDA) are intercepted at the edges of the IMCs, whereas no significant dislocations and deformations are observed in the IMCs. Therefore, more dislocations and deformations can be generated in the NDA, thereby resulting in increased plasticity. Moreover, the increase in strength comes from the following three aspects: (1) the refinement of grains leads to more grain boundaries and the dislocation movement receives more obstruction, which enhances the strength. (2) The pinning effect of IMC causes more dislocations in the NDA, which further makes the dislocation movement receive obstruction and enhances the strength. (3) The plastic flow of nano-amorphous leads to deformation hardening [19], thereby enhancing the strength.

Fig. 4f shows the structure of the NDA and a schematic diagram of the soft–hard phase reinforcement, showing that the nanocrystals within the NDA are randomly embedded in the amorphous regions. During plastic deformation, dislocations or rotations generated by the nanocrystals within the NDA are deformed, resulting in strain hardening and plasticity. With the increase of load, nano-amorphous flows and increases plasticity [18,19]. Moreover, the dislocations generated within the NDA are hindered by the IMC phase (Fig. 4e), which results in more dislocations and deformations that can be generated in the NDA, leading to strain strengthening and increased plasticity.

CONCLUSION

We present a new strategy for designing $Al_{80}Li_5Mg_5Zn_5Cu_5$ nano-amorphous–crystalline dual-phase alloy with superior properties. The nano-amorphous phase shows good thermal stability during fabrication and mechanical testing above the crystallization temperature. During plastic deformation, dislocations, rotational deformation of nanocrystals in NDA, and plastic flow of amorphous occur, leading to increased plasticity and strain hardening. Moreover, the "pinning" effect of IMCs

leads to more strain in NDA. Consequently, the unique structure increases the true fracture strength of $Al_{80}Li_5Mg_5Zn_5Cu_5$ NDMA from 528 to 657 MPa and the true strain from 18% to 48%. In addition, the yield strength of $Al_{80}Li_5Mg_5Zn_5Cu_5$ NDMA at 250°C is 1.5 times higher than that of commonly used high-strength aluminum alloys. Therefore, this alloy is suitable for lightweight, high-performance alloy materials in extreme environments.

Received 20 October 2021; accepted 14 December 2021; published online 28 February 2022

1 Raabe D, Tasan CC, Olivetti EA. Strategies for improving the sustainability of structural metals. Nature, 2019, 575: 64–74
2 Li Z, Pradeep KG, Deng Y, *et al.* Metastable high-entropy dual-phase alloys overcome the strength–ductility trade-off. Nature, 2016, 534: 227–230
3 Ritchie RO. The conflicts between strength and toughness. Nat Mater, 2011, 10: 817–822
4 Wei Y, Li Y, Zhu L, *et al.* Evading the strength–ductility trade-off dilemma in steel through gradient hierarchical nanotwins. Nat Commun, 2014, 5: 3580
5 Shi P, Zhong Y, Li Y, *et al.* Multistage work hardening assisted by multi-type twinning in ultrafine-grained heterostructural eutectic high-entropy alloys. Mater Today, 2020, 41: 62–71
6 Jiao ZB, Luan JH, Miller MK, *et al.* Precipitation mechanism and mechanical properties of an ultra-high strength steel hardened by nanoscale NiAl and Cu particles. Acta Mater, 2015, 97: 58–67
7 Kim SH, Kim H, Kim NJ. Brittle intermetallic compound makes ultrastrong low-density steel with large ductility. Nature, 2015, 518: 77–79
8 Fleischer RL, Zabala RJ. Mechanical properties of diverse binary high-temperature intermetallic compounds. Metall Trans A, 1990, 21: 2709–2715
9 Jiang S, Wang H, Wu Y, *et al.* Ultrastrong steel *via* minimal lattice misfit and high-density nanoprecipitation. Nature, 2017, 544: 460–464
10 Yang T, Zhao YL, Tong Y, *et al.* Multicomponent intermetallic nanoparticles and superb mechanical behaviors of complex alloys. Science, 2018, 362: 933–937
11 Wu G, Chan KC, Zhu L, *et al.* Dual-phase nanostructuring as a route to high-strength magnesium alloys. Nature, 2017, 545: 80–83
12 He G, Eckert J, Löser W, *et al.* Novel Ti-base nanostructure–dendrite composite with enhanced plasticity. Nat Mater, 2003, 2: 33–37
13 Gertsman VY, Birringer R. On the room-temperature grain growth in nanocrystalline copper. Scripta Metall Mater, 1994, 30: 577–581
14 Wang JQ, Shen Y, Perepezko JH, *et al.* Increasing the kinetic stability of bulk metallic glasses. Acta Mater, 2016, 104: 25–32
15 Singh S, Ediger MD, de Pablo JJ. Ultrastable glasses from in SiLiCo vapour deposition. Nat Mater, 2013, 12: 139–144
16 Wu G, Balachandran S, Gault B, *et al.* Crystal–glass high-entropy nanocomposites with near theoretical compressive strength and large deformability. Adv Mater, 2020, 32: 2002619
17 Wu G, Liu C, Sun L, *et al.* Hierarchical nanostructured aluminum alloy with ultrahigh strength and large plasticity. Nat Commun, 2019, 10: 5099
18 Guo H, Yan PF, Wang YB, *et al.* Tensile ductility and necking of metallic glass. Nat Mater, 2007, 6: 735–739
19 Jang D, Greer JR. Transition from a strong-yet-brittle to a stronger-and-ductile state by size reduction of metallic glasses. Nat Mater, 2010, 9: 215–219
20 Hofmann DC, Suh JY, Wiest A, *et al.* Designing metallic glass matrix composites with high toughness and tensile ductility. Nature, 2008, 451: 1085–1089
21 Schawe JEK, Löffler JF. Existence of multiple critical cooling rates which generate different types of monolithic metallic glass. Nat Commun, 2019, 10: 1
22 Gangopadhyay AK, Croat TK, Kelton KF. The effect of phase separation on subsequent crystallization in $Al_{88}Gd_6La_2Ni_4$. Acta Mater, 2000, 48: 4035–4043
23 Li H, Wang A, Liu T, *et al.* Design of Fe-based nanocrystalline alloys with superior magnetization and manufacturability. Mater Today, 2021, 42: 49–56
24 Greer AL. Confusion by design. Nature, 1993, 366: 303–304
25 George EP, Raabe D, Ritchie RO. High-entropy alloys. Nat Rev Mater, 2019, 4: 515–534
26 Guo S, Liu CT. Phase stability in high entropy alloys: Formation of solid-solution phase or amorphous phase. Prog Nat Sci-Mater Int, 2011, 21: 433–446
27 Huang Z, Dai Y, Li Z, *et al.* Investigation on surface morphology and crystalline phase deformation of $Al_{80}Li_5Mg_5Zn_5Cu_5$ high-entropy alloy by ultra-precision cutting. Mater Des, 2020, 186: 108367
28 Li R, Li X, Ma J, *et al.* Sub-grain formation in Al–Li–Mg–Zn–Cu lightweight entropic alloy by ultrasonic hammering. Intermetallics, 2020, 121: 106780
29 Udoye NE, Inegbenebor AO, Fayomi OSI. The study on improvement of aluminium alloy for engineering application: A review. Int J Mech Eng Technol, 2019, 10: 380–385
30 Dursun T, Soutis C. Recent developments in advanced aircraft aluminium alloys. Mater Des (1980-2015), 2014, 56: 862–871
31 Lee H, Choi JH, Jo MC, *et al.* Effects of SiC particulate size on dynamic compressive properties in 7075-T6 Al-SiCp composites. Mater Sci Eng-A, 2018, 738: 412–419
32 Öz T, Karaköse E, Keskin M. Impact of beryllium additions on thermal and mechanical properties of conventionally solidified and melt-spun Al–4.5wt.%Mn–*x*wt.%Be (*x*=0, 1, 3, 5) alloys. Mater Des, 2013, 50: 399–412
33 Zupanič F, Gspan C, Burja J, *et al.* Quasicrystalline and L12 precipitates in a microalloyed Al-Mn-Cu alloy. Mater Today Commun, 2020, 22: 100809
34 Taheri-Mandarjani M, Zarei-Hanzaki A, Abedi HR. Hot ductility behavior of an extruded 7075 aluminum alloy. Mater Sci Eng-A, 2015, 637: 107–122
35 Liu W, Zhao H, Li D, *et al.* Hot deformation behavior of aa7085 aluminum alloy during isothermal compression at elevated temperature. Mater Sci Eng-A, 2014, 596: 176–182
36 Nath Verma T, Banerjee M, Nashine P. Hot compression test of aa 2014 aluminum alloy with microstructure analysis and processing maps. Mater Today-Proc, 2018, 5: 7247–7255
37 Yang Y, Peng X, Ren F, *et al.* Constitutive modeling and hot deformation behavior of duplex structured Mg–Li–Al–Sr alloy. J Mater Sci Tech, 2016, 32: 1289–1296
38 Wang CY, Wu K, Zheng MY. Hot deformation behavior of $Al_{18}B_4O_{33}$w/ZK60 magnesium matrix composite. Mater Sci Eng-A, 2008, 487: 495–498
39 He H, Yi Y, Cui J, *et al.* Hot deformation characteristics and processing parameter optimization of 2219 Al alloy using constitutive equation and processing map. Vacuum, 2019, 160: 293–302
40 Hansen N. Hall–petch relation and boundary strengthening. Scripta Mater, 2004, 51: 801–806
41 Hall EO. The deformation and ageing of mild steel: III Discussion of results. Proc Phys Soc B, 1951, 64: 747–753
42 Petch N. The cleavage strength of polycrystals. J Iron Steel Res Int, 1953, 174: 25–28
43 Liu YH, Wang G, Wang RJ, *et al.* Super plastic bulk metallic glasses at room temperature. Science, 2007, 315: 1385–1388
44 Li YY, Yang C, Chen WP, *et al.* Ultrafine-grained $Ti_{66}Nb_{13}Cu_8Ni_{6.8}Al_{6.2}$ composites fabricated by spark plasma sintering and crystallization of amorphous phase. J Mater Res, 2009, 24: 2118–2122
45 Li YY, Yang C, Qu SG, *et al.* Nucleation and growth mechanism of crystalline phase for fabrication of ultrafine-grained $Ti_{66}Nb_{13}Cu_8Ni_{6.8}Al_{6.2}$ composites by spark plasma sintering and crystallization of amorphous phase. Mater Sci Eng-A, 2010, 528: 486–493
46 Lee TC, Chan LC, Wu BJ. Straining behaviour in blanking process-fine blanking *vs* conventional blanking. J Mater Proc Tech, 1995, 48: 105–111
47 Murayama M, Howe JM, Hidaka H, *et al.* Atomic-level observation of disclination dipoles in mechanically milled, nanocrystalline Fe. Science, 2002, 295: 2433–2435

48 Ovid'ko IA. Deformation of nanostructures. Science, 2002, 295: 2386
49 Volkert CA, Donohue A, Spaepen F. Effect of sample size on deformation in amorphous metals. J Appl Phys, 2008, 103: 083539

Acknowledgements This work was supported by the Key Basic and Applied Research Program of Guangdong Province, China (2019B030302010), the National Natural Science Foundation of China (52122105 and 51871157), the National Key Research and Development Program of China (2018YFA0703604). Thanks to Dr. Tong Xing from Guangdong Songshan Lake Materials Laboratory for his contribution to the TEM in-situ heating experiments.

Author contributions Li H and Ma J conceived the experiments. Li H, Fu J, Cai W, and Yan Y performed the experiments. Yang C analyzed the data. Li H and Ma J wrote the manuscript with contributions from other authors.

Conflict of interest The authors declare no conflict of interest.

Supplementary information Experimental details and supporting data are available in the online version of the paper.

Hongzhen Li received his master degree in mechanical engineering from Shenzhen University (SZU) in 2020. Currently, he is studying for a PhD at South China University of Technology. His research includes metallic glass, high-entropy alloys and advanced manufacturing.

Jiang Ma received his BSc degree in materials science and engineering from Southeast University in 2009 and PhD degree from the Institute of Physics, Chinese Academy of Sciences (CAS), in 2014. He is currently a Professor at the College of Mechatronics and Control Engineering, SZU. His research includes metallic glass, high-entropy alloy, micro/nano precision forming, and functional surface fabrication and application.

$Al_{80}Li_5Mg_5Zn_5Cu_5$多组元合金的纳米非晶-晶态双相设计

李泓臻[1], 杨超[2], 傅佳男[1], 蔡潍锶[2], 闫玉强[3], 马将[1*]

摘要 设计具有高强度、高延展性和高热稳定性的金属材料，一直是材料科学界追求的目标. 强度和延展性之间的平衡始终面临挑战. 本文中，我们以$Al_{80}Li_5Mg_5Zn_5Cu_5$多组元合金为模型，提出了一种设计并制造大块非晶-结晶双相优质合金的新策略. 得到的$Al_{80}Li_5Mg_5Zn_5Cu_5$纳米非晶双相合金的真实断裂强度从528 MPa提高到657 MPa，真实应变从18%提高到48%. 纳米非晶相在热制造和高于结晶温度的力学性能测试中展现出优异的热稳定性，使得该合金在250°C时的屈服强度，比常用的高强度铝合金高出1.5倍. 这一策略为高性能合金的设计、制造提供了一种新的方法和概念.